

IMPLICIT DYNAMICAL FLOW FUSION (IDFF) FOR GENERATIVE MODELING

Anonymous authors
Paper under double-blind review

ABSTRACT

Conditional Flow Matching (CFM) models can generate high-quality samples from a non-informative prior, but they can be slow, often needing hundreds of network evaluations (NFE). To address this, we propose Implicit Dynamical Flow Fusion (IDFF); IDFF learns a new vector field with an additional momentum term that enables taking longer steps during sample generation while maintaining the fidelity of the generated distribution. Consequently, IDFFs reduce the NFEs by a factor of ten (relative to CFMs) without sacrificing sample quality, enabling rapid sampling and efficient handling of image and time-series data generation tasks. We evaluate IDFF on standard benchmarks such as CIFAR-10 and CelebA for image generation, where we achieve likelihood and quality performance comparable to CFMs and diffusion-based models with fewer NFEs. IDFF also shows superior performance on time-series datasets modeling, including molecular simulation and sea surface temperature (SST) datasets, highlighting its versatility and effectiveness across different domains.

1 INTRODUCTION

Diffusion models have emerged as powerful tools for modeling complex, high-dimensional data by iteratively transforming random noise into meaningful information (Cachay et al., 2023; Myers et al., 2022). These models have demonstrated remarkable success in various domains, including high-quality image generation (Song et al., 2020a) and text production (Liu et al., 2024; Kim et al., 2019). However, their training process remains computationally intensive, often requiring hundreds of function evaluations (NFEs) to achieve high-quality results (Ho et al., 2020). While techniques such as DPM-solver (Lu et al., 2022a;b) and Denoising Diffusion Implicit Models (DDIMs) (Song et al., 2020b) have made strides in reducing NFEs for diffusion-based generative models, significant computational challenges persist.

In contrast to diffusion models, which parameterize the dynamics of noise-to-data transformation, Conditional Flow Matching (CFMs) directly parameterize vector fields governing this transformation (Liu et al., 2022; Albergo and Vanden-Eijnden, 2022; Albergo et al., 2023). CFMs leverage the change of variable theory in statistics to define conditional probability paths, enabling faster convergence during training compared to diffusion models (Lipman et al., 2022). However, generating high-quality samples with CFMs still requires hundreds of NFEs, making the process computationally expensive (Dao et al., 2023) and limiting the extension of CFM models to time-series data modeling, as NFEs scale with sequence length.

To address these challenges, we introduce a novel method to enhance the efficiency of CFMs, allowing for longer sampling steps without compromising the fidelity of the target distribution. Our approach draws inspiration from Hamiltonian Monte Carlo (HMC) algorithms (Neal, 2012a; Neal et al., 2011), which utilize the conservation properties of Hamiltonian dynamics to couple target and momentum variables. The key contributions of our work are as follows:

1. We propose Implicit Dynamical Flow Fusion (IDFF), which integrates a momentum term into the vector field of conditional flow models. Similar to how HMC reduces the number of samples required to reach the target distribution (Neal, 2012a; Neal et al., 2011), **IDFF reduces the NFE by a factor of 10 compared to traditional CFMs** while maintaining identical marginal

054
055
056
057
058
059
060
061
062
063
064
065
066
067
068
069
070
071
072
073
074
075
076
077
078
079
080
081
082
083
084
085
086
087
088
089
090
091
092
093
094
095
096
097
098
099
100
101
102
103
104
105
106
107

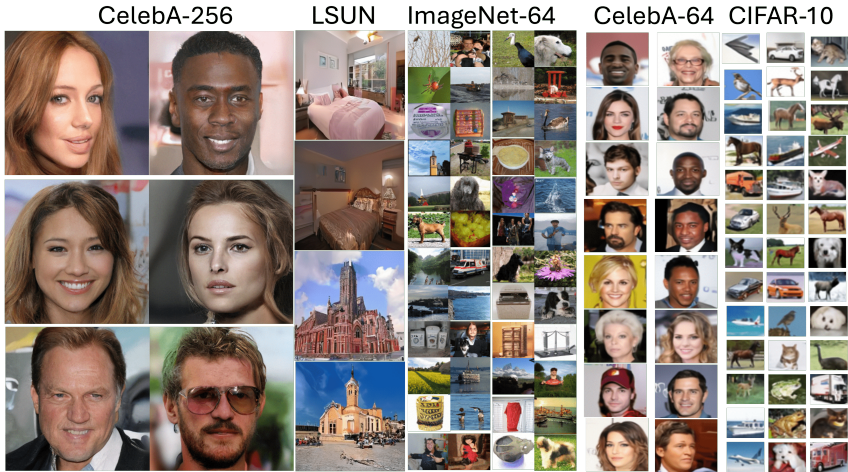


Figure 1: Image generation using IDFF (with NFE=10) applied to multiple datasets: CIFAR10, CelebA-64, ImageNet-64, LSUN-Bedroom, LSUN-Church, and CelebA-HQ. The quality of the generated images demonstrates IDFF’s ability to capture and reproduce realistic visuals across varying levels of complexity and resolution. Additional samples and further analysis can be found in Appendix A.6.

- distributions. Additionally, we introduce a training objective that directly aligns generated samples with actual data rather than solely focusing on matching conditional flows.
2. We validate IDFF through extensive experiments on image generation using datasets such as CIFAR-10 and CelebA. Additional results on ImageNet-64, CelebA-HQ, LSUN-Church, and LSUN-Bedroom are presented in Figure 1. Our models achieve a superior balance between computational cost and sample quality compared to both traditional diffusion models (e.g., DDPM (Ho et al., 2020), DDIM (Song et al., 2020b)) and current CFMs.
 3. We demonstrate that reducing NFEs makes IDFF practical for other generation tasks, such as time-series modeling. We showcase IDFF’s effectiveness in capturing complex dynamical systems, including 3D attractors, molecular dynamics (MD), and sea surface temperatures (SST). Our results indicate that IDFF surpasses other methods in sample quality for MD and SST datasets while maintaining computational efficiency, with $NFE \leq 5$ for each generated sample.

2 BACKGROUND

Score-based generative models. Let $p_{\text{data}} = \{\mathbf{x}^1, \mathbf{x}^2, \dots, \mathbf{x}^N\}$, where $\mathbf{x}^i \stackrel{\text{iid}}{\sim} p(\mathbf{x})$ and $\mathbf{x}^i \in \mathbb{R}^d$ for all $i = 1, 2, \dots, N$. We aim to build a generative model for this dataset given empirical samples. Moving forward, we suppress the superscript on each \mathbf{x}^i .

Score-based models (Song and Ermon, 2019) represent a broad class of diffusion models that describe a continuous-time stochastic process characterized by a stochastic process \mathbf{x}_t , which is governed by the following Itô stochastic differential equation (SDE):

$$d\mathbf{x}_t = \mathbf{f}(\mathbf{x}_t, t)dt + g(t)d\mathbf{w}, \tag{1}$$

where $t \in [0, 1]$, $\mathbf{f}(\cdot, t) : \mathbb{R}^d \rightarrow \mathbb{R}^d$ is the drift coefficient, $g(\cdot) : \mathbb{R} \rightarrow \mathbb{R}$ is the diffusion coefficient of \mathbf{x}_t , and $\mathbf{w} \in \mathbb{R}^d$ is a standard Wiener process.

The time-reversed version of this diffusion process, derived from the Fokker–Planck equations (Song and Ermon, 2019), is also a diffusion process. This reverse-time SDE is defined as:

$$d\mathbf{x}_t = (\mathbf{f}(\mathbf{x}_t, t) - g(t)^2 \nabla_{\mathbf{x}_t} \log p_t(\mathbf{x}_t)) dt + g(t)d\bar{\mathbf{w}}, \tag{2}$$

where $\bar{\mathbf{w}}$ is a standard Wiener process. Equation 2 produces the same marginal distributions as the forward diffusion process defined by Equation 1.

Equation 2 must be solved to generate samples from this model. The score-matching approach simplifies this process by redefining $\mathbf{f}(\mathbf{x}_t, t) = h(t)\mathbf{x}_t$, where $h : \mathbb{R} \rightarrow \mathbb{R}$ typically assumes an affine form, such as $\mathbf{f}(\mathbf{x}_t, t) = \mathbf{x}_t$. Moreover, $g(\cdot)$, which governs the noise intensity added to the process, often follows a linear or exponential schedule in time.

This reformulation enables a simplification of solving Equation 2 by focusing solely on learning $\nabla_{\mathbf{x}} \log p_t(\mathbf{x}_t)$ for all t . With this approach, and initializing with random noise, e.g., $\mathbf{x}_0 \sim \mathcal{N}(0, \mathbf{I})$, the process gradually converges to the data distribution p_{data} , reaching it at $t = 1$.

(Conditional) Flow Matching (CFM). Flow-matching (FM) transforms a simple prior distribution into a complex target distribution. FM is defined by a time-dependent vector field \mathbf{v}_t , which governs the dynamics of an ordinary differential equation (ODE):

$$\frac{d}{dt}(\mathbf{x}_t) = \mathbf{v}_t(\mathbf{x}_t) \quad (3)$$

The solution to this ODE, represented by $\phi(\mathbf{x}_t)$, evolves along the vector field \mathbf{v}_t from time 0 to time 1, producing $\mathbf{x}_1 \sim p_1$. As samples move along the vector field \mathbf{v}_t , $p_t(\mathbf{x}_t)$ changes over time, described by the continuity equation.

$$\frac{\partial p_t}{\partial t} = -\nabla \cdot (p_t \mathbf{v}_t) \quad (4)$$

where $p_t(\mathbf{x}_t)$ is determined by $\mathbf{v}_t(\mathbf{x}_t)$, $\nabla \cdot$ is the divergence operator, with $p_1 \approx p_{\text{data}}$.

If the probability path $p_t(\mathbf{x}_t)$ and the vector field $\mathbf{v}_t(\mathbf{x}_t)$ are given, and if $p_t(\mathbf{x}_t)$ can be efficiently sampled, we can then define a parameterized vector field $\hat{\mathbf{v}}_t(\mathbf{x}_t; \theta)$ using a neural network with weights θ . This parameterized vector field approximates $\mathbf{v}_t(\mathbf{x}_t)$, and our goal is to learn how to generate samples from the ODE defined in equation 3. The parameters of the neural network are trained using the following objective: $\mathcal{L}_{\text{FM}}(\theta) := \mathbb{E}_{t \sim \mathcal{U}(0,1), \mathbf{x}_t \sim p_t(\mathbf{x}_t)} \|\hat{\mathbf{v}}_t(\mathbf{x}_t; \theta) - \mathbf{v}_t(\mathbf{x}_t)\|^2$ to solve the ODE defined in equation 3. Here, $\mathbf{v}_t(\mathbf{x}_t)$ can be defined as $\mathbf{v}_t(\mathbf{x}_t) := \mathbb{E}_{q(\mathbf{z})} \left[\frac{\mathbf{v}_t(\mathbf{x}_t | \mathbf{z}) p_t(\mathbf{x}_t | \mathbf{z})}{p_t(\mathbf{x}_t)} \right]$ with some conditional variable \mathbf{z} with distribution $q(\mathbf{z})$; refer to Theorem 3.1 in Tong et al. (2023a) for more details.

However, this learning objective becomes intractable for general source and target distributions. To mitigate this, we can focus on cases where the conditional probability paths $p_t(\mathbf{x}_t | \mathbf{x}_1)$ and vector fields $\mathbf{v}_t(\mathbf{x}_t | \mathbf{x}_1)$ associated with $p_t(\mathbf{x}_t)$ and $\mathbf{v}_t(\mathbf{x}_t)$ are known and have simple forms (Tong et al., 2023b). In such cases, we can recover the vector field $\mathbf{v}_t(\mathbf{x}_t)$ using an unbiased stochastic objective known as the Conditional Flow Matching (CFM) loss, defined as:

$$\mathcal{L}_{\text{CFM}}(\theta) := \mathbb{E}_{t, \mathbf{x}_1, \mathbf{x}_t} \|\hat{\mathbf{v}}_t(\mathbf{x}_t | \mathbf{x}_1; \theta) - \mathbf{v}_t(\mathbf{x}_t)\|^2 \quad (5)$$

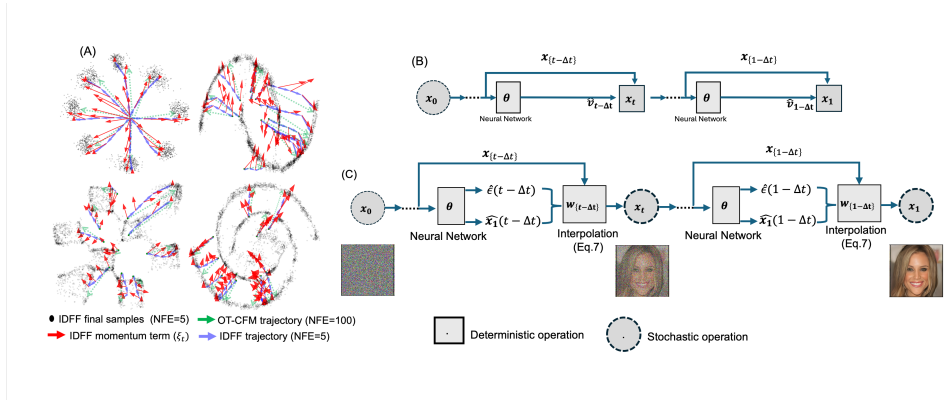
where $t \sim \mathcal{U}[0, 1]$, $\mathbf{x}_1 \sim p_{\text{data}}$, and $\mathbf{x}_t \sim p_t(\mathbf{x}_t | \mathbf{x}_1)$. The training objective in Equation 5 ensures that the marginalized vector field $\hat{\mathbf{v}}_t(\mathbf{x}_t | \mathbf{x}_1; \theta)$, denoted as $\hat{\mathbf{v}}_t(\mathbf{x}_t)$, generates $p_t(\mathbf{x}_t)$, similar to FM models.

CFMs vs Diffusion Models. CFMs share similarities with diffusion models; both rely on defining continuous probability paths over time. However, diffusion models use stochastic processes to transform data distributions, typically governed by an SDE. However, CFMs utilize a vector field to directly map an initial prior distribution to the target distribution via a deterministic process (Equation 4). Diffusion models, such as denoising score matching models, rely on stochastic diffusion paths to approximate the data distribution. CFMs bypass this stochastic process by constructing a conditional vector field and sampling from the ODE defined in Equation 3.

Optimal Transport CFMs (OT-CFMs). The CFM objective defined in Equation 5 appears simple. However, it is nearly intractable due to the absence of prior knowledge regarding an appropriate mapping that links between the initial (p_0) and target (p_{data}) distributions. To address this challenge, optimal transport (OT) (Tong et al., 2020) is used to couple the initial and target distributions. This approach seeks a mapping from p_0 to p_1 that minimizes the displacement cost between these two distributions, resulting in flows that can be integrated accurately. This CFM variant is known as Optimal Transport CFMs (OT-CFMs), and the conditional vector field corresponds to this is

162 $\hat{\mathbf{v}}_t(\mathbf{x}_t|\mathbf{x}_1) = \frac{\mathbf{x}_1 - \mathbf{x}_t}{1-t}$. While OT improves training efficiency in CFMs, traditional sampling methods
 163 for CFMs require over a hundred function evaluations (NFE) to produce high-quality samples (Tong
 164 et al., 2023a). The lack of flexibility in sampling steps during training further limits their ability to
 165 efficiently generate samples, often resulting in a high NFE.

166 Additionally, the OT-CFM vector field, which can be reformulated as $\hat{\mathbf{v}}_t(\mathbf{x}_t|\mathbf{x}_1) = \mathbf{x}_1 - \mathbf{x}_t$ Pooladian
 167 et al. (2023), focuses on exactly transporting all points \mathbf{x}_0 to \mathbf{x}_1 along straight-line paths. This
 168 implies that all points along the path from 0 to t means that the transport map shares the same
 169 regression weights when training with the $\mathcal{L}_{\text{CFM}}(\theta)$ objective. However, this uniform weighting
 170 across the trajectory may overlook that points closer to $t = 1$ need finer attention to detail and,
 171 consequently, a more complex flow; this may limit the model’s ability to effectively represent
 172 complex structures in the final generated samples. Furthermore, the deterministic sample generation
 173 in CFMs, $\mathbf{x}_t = \mathbf{x}_{t-\Delta t} + \Delta t \hat{\mathbf{v}}_t(\mathbf{x}_t; \theta)$ (see Figure 2.B for visualization), may restrict the flexibility
 174 of CFM, as it prevents the introduction of stochasticity that could otherwise enhance the diversity
 175 and richness of generated samples. This might manifest in a lack of expressiveness when generating
 176 fine-grained or high-dimensional data. These limitations underscore the need for new approaches to
 177 sample diversity and NFE of CFMs. Our paper tackles these limitations by proposing an alternative
 178 vector field that better balances deterministic transport with elements of stochasticity to improve
 179 sample quality.



193
 194 Figure 2: A) Comparison of trajectory sampling between IDFF and OT-CFMs: The figure displays
 195 4096 final samples generated by IDFF. As shown, IDFF takes larger steps toward the target distribution,
 196 guided by the momentum term. While OT-CFM follows a nearly straight path to reach the target
 197 distribution, it requires a higher number of function evaluations (NFEs). B) OT-CFMs sampling
 198 process. C) IDFF sampling process. In this process, $\hat{\mathbf{x}}_1(\cdot)$ approximates the data sample \mathbf{x}_1 , $\hat{\epsilon}(\cdot)$
 199 approximates the scores associated with ξ_t , and $\mathbf{w}_t(\cdot)$ is the calculated vector field by equation 7.
 200 For further details, see Algorithm 2. The key difference between IDFF and OT-CFMs is that instead
 201 of directly generating the vector field with, IDFF generates $\hat{\mathbf{x}}_1(\cdot)$ and $\hat{\epsilon}(\cdot)$, and then reconstructs
 202 the vector field, following it. Additionally, IDFF uses a Gaussian distribution to sample \mathbf{x}_t rather than
 203 calculating it deterministically.

204
 205 **Hamiltonian Monte Carlo (HMC).** HMC is a powerful sampling algorithm designed to improve ef-
 206 ficiency in exploring complex probability distributions by introducing auxiliary momentum variables.
 207 In HMC, particle dynamics are simulated in a potential field using Hamiltonian dynamics, which
 208 describe the total energy of a system through the Hamiltonian function $H(\mathbf{x}, \mathbf{p}) = U(\mathbf{x}) + K(\mathbf{p})$.
 209 \mathbf{x} represents the position, \mathbf{p} represents momentum, $U(\mathbf{x})$ represents the potential energy related to
 210 the target distribution, and $K(\mathbf{p}) = \frac{1}{2} \mathbf{p}^T \mathbf{M}^{-1} \mathbf{p}$ is the kinetic energy, with \mathbf{M} being the mass matrix.
 211 The dynamics of this system evolve according to:

$$212 \frac{d\mathbf{x}}{dt} = \nabla_{\mathbf{p}} H(\mathbf{x}, \mathbf{p}) = \mathbf{M}^{-1} \mathbf{p}, \quad \frac{d\mathbf{p}}{dt} = -\nabla_{\mathbf{x}} H(\mathbf{x}, \mathbf{p}) = -\nabla U(\mathbf{x}).$$

213
 214 These dynamics preserve the system’s total energy, enabling efficient exploration of the probability
 215 space. HMC achieves this by leveraging momentum to facilitate directed movement, reducing random
 walk behavior, and overcoming local energy barriers. These properties lead to faster convergence to

the target distribution with fewer function evaluations. HMC generates a sample from some target distributions by following Hamiltonian dynamics in an extended state space (\mathbf{x}, \mathbf{p}) . IDFF attempts to design a flow-matching procedure with a similar intuition.

3 IMPLICIT DYNAMICAL FLOW FUSION MODEL (IDFF)

IDFF aims to improve sampling efficiency while enhancing sample quality of OT-CFMs through two key innovations: (1) the incorporation of a learnable Hamiltonian momentum term, ξ_t , into the conditional vector field, which enhances sampling efficiency; and (2) the proposal of a new objective function that learns the IDFF’s vector field in input space.

3.1 LEARNING CFMS WITH MOMENTUM

To improve sampling efficiency while preserving distribution accuracy in CFMs, we introduce a learnable Hamiltonian momentum term, ξ_t , integrated with the original vector field $\mathbf{v}_t(\mathbf{x}_t)$. This integration yields a new, more flexible vector field:

$$\tilde{\mathbf{v}}_t(\mathbf{x}_t) = \sqrt{1 - \sigma_t^2} \mathbf{v}_t(\mathbf{x}_t) + \sigma_t^2 \xi_t, \quad (6)$$

where σ_t is a time-dependent interpolation factor balancing \mathbf{v}_t and ξ_t .

Interpolating the vector field: We define the interpolation factor σ_t as $\sigma_t = \sigma_0 \sqrt{t(1-t)}$, where σ_0 is a hyperparameter that controls the overall influence of the momentum term. While the IDFF vector field converges to OT-CFMs in either limit, outside of it, it enables the flow to leverage the momentum variables to guide the flow based on the momentum variables. Our empirical results demonstrate that this approach significantly improves sampling efficiency by substantially reducing the NFEs required. Our approach also overcomes the limitations of uniform weighting across trajectories by prioritizing samples near $t = 0, 1$, allowing finer attention to complex structures; see Figure 2.A.

Designing momentum variables: The term ξ_t is designed to guide the new vector field toward the correct probability flow for the next time step, ensuring its role in accurately modeling the distribution. There are many potential choices to make here. Still, we take inspiration from Hamiltonian Monte Carlo, which showcases how to leverage momenta to sample complex multi-modal posterior distributions rapidly Neal (2012b). A potential design for ξ_t is $\xi_t = \gamma \nabla_x \log p_t(\mathbf{x}_t)$, which aligns with the gradient of the log probability of the samples \mathbf{x}_t . If $p_t(\mathbf{x}_t | \mathbf{x}_1)$ is a Gaussian with variance σ_t^2 , ξ_t can be simplified to $-\frac{\epsilon_0}{\sigma_t}$, where $\epsilon_0 \sim \mathcal{N}(0, 1)$. ξ_t directs the flow similarly to HMC’s momentum, promoting efficient exploration of complex distributions. The theoretical connection between HMC and IDFF can be understood through their respective probability flows. HMC generates samples by following Hamiltonian dynamics in an extended state space (\mathbf{x}, \mathbf{p}) . In contrast, IDFF’s probability flow operates directly in the sample space while incorporating momentum-like behavior through ξ_t . Both methods use auxiliary variables to enhance sampling efficiency and preserve the desired target distribution. Alternatively, higher-order choices for momentum terms could capture even more complex interactions in the flow. $\xi_t = \gamma \nabla_x \log p_t(\mathbf{x}_t)$ drives the vector field toward regions of high probability, thereby improving the accuracy of the generated samples. γ serves as a weighting factor that controls the influence of this term.

To maintain the same probability path as the original CFM, the vector field must satisfy the continuity constraint defined in equation 4. By incorporating $\tilde{\mathbf{v}}_t(\mathbf{x}_t)$ into the continuity equation 4 (detailed in Appendix A.1.1), we derive the IDFF probability flow ODE:

$$\mathbf{w}_t(\mathbf{x}_t) = \tilde{\mathbf{v}}_t(\mathbf{x}_t) - \frac{\sigma_t^2}{2} \nabla \log p_t(\mathbf{x}_t) = \sqrt{1 - \sigma_t^2} \mathbf{v}_t(\mathbf{x}_t) + \frac{(2\gamma - 1)}{2} \sigma_t^2 \nabla \log p_t(\mathbf{x}_t), \quad (7)$$

To ensure that our new marginal vector field $\mathbf{w}_t(\mathbf{x}_t)$ converges to the standard $\mathbf{v}_t(\mathbf{x}_t)$ at the start and end points of the process, σ_t must approach zero as $t \rightarrow 0, 1$. This convergence is crucial for maintaining consistent marginal distributions at these points.

Therefore, $\mathbf{w}_t(\mathbf{x}_t)$ now replaces the vector field $\mathbf{v}(\mathbf{x}_t)$ in the probability flow ODE (equation 3), enabling the construction of a new generative process that follows the same probability path $p_t(\mathbf{x}_t)$. This process starts with $\mathbf{x}_0 \sim \mathcal{N}(0, \mathbf{I})$ and follows $p_t(\mathbf{x}_t)$ to produce \mathbf{x}_1 . The resulting model thus *implicitly* models the score function using flow matching which motivates the name *Implicit Diffusion Flow Fusion*.

Lemma 1. Given that $\mathbf{v}_t(\mathbf{x}_t)$ generates $p_t(\mathbf{x}_t)$ and σ_t approaches 0 for $t \in 0, 1$, the IDFF probability flow ODE (Eq. 7) follows the same marginal distribution as the CFMs with the ODE defined in equation 3.

Proof Schema for Lemma 1. Our goal is to show that the IDFF probability flow ODE shares the same marginal distribution as CFMs when σ_t is small for $t \in 0, 1$.

- **Step 1: Define the vector fields.** We introduce $\tilde{\mathbf{v}}_t(\mathbf{x}_t)$ governed by the ξ_t and $\mathbf{v}_t(\mathbf{x}_t)$ from the original CFM.
- **Step 2: Apply the continuity equation.** By substituting $\tilde{\mathbf{v}}_t(\mathbf{x}_t)$ into the continuity equation, we derive the IDFF ODE, $\mathbf{w}_t(\mathbf{x}_t)$.
- **Step 3: Analyze boundary conditions.** We show that at $t = 0$ and $t = 1$, where σ_t approaches 0, the IDFF ODE converges to the CFM-ODE, ensuring the same marginal distributions.

□

Appendix A.1.1 provides the complete proof. This lemma and its proof establish the consistency of IDFF concerning existing CFMs. The approach showcases how to design a new flow augmented with momentum variables with an interpolant that guarantees that it matches OT-CFM in the limit. In what follows, we discuss how to parameterize and learn such a flow.

3.2 LEARNING FLOWS IN INPUT SPACE

One of the challenges in our formalism is learning \mathbf{w}_t . This challenge arises because \mathbf{v}_t operates in vector space while ξ_t remains in the input space. Rather than training one part of the model in vector space and the other in input space, we define a new objective defined entirely within the input space to address this. Learning the vector field in the input space implies optimizing the vector itself, which is the reasoning behind naming the IDFF model an implicit model of dynamical flows. We begin by defining an OT path $p_t(\mathbf{x}_t|\mathbf{x}_1)$, which acts as a probability bridge between \mathbf{x}_0 and \mathbf{x}_1 . This path is a stochastic interpolator between the source \mathbf{x}_1 and target \mathbf{x}_0 , as follows:

$$p_t(\mathbf{x}_t|\mathbf{x}_1) = \mathcal{N}(\mathbf{x}_t | t\mathbf{x}_1 + (1-t)\mathbf{x}_0, \sigma_t^2\mathbf{I}), \quad \sigma_t = \sigma_0\sqrt{t(1-t)} \quad (8)$$

The corresponding conditional vector field is given by:

$$\hat{\mathbf{v}}_t(\mathbf{x}_t|\mathbf{x}_1) = \frac{\mathbf{x}_1 - \mathbf{x}_t}{1-t} \quad (9)$$

This definition aligns with the conditional OT paths between \mathbf{x}_1 and \mathbf{x}_0 . For large datasets, computing this OT map can be challenging. We employ a minibatch approximation of OT to address this, similar to (Fratras et al., 2021). While this introduces some errors compared to the exact OT solution, it has proven effective in numerous applications such as domain adaptation and generative modeling (Genevay et al., 2018).

Current CFM objectives typically use a loss function (defined in equation 5) that optimizes the prediction of the vector field. We propose an alternative approach: defining a denoising neural network $\hat{\mathbf{x}}_1(\mathbf{x}_t, t; \theta)$ and reparameterizing $\hat{\mathbf{v}}_t(\mathbf{x}_t | \mathbf{x}_1; \theta)$ as follows:

$$\hat{\mathbf{v}}_t(\mathbf{x}_t | \mathbf{x}_1; \theta) = \frac{\hat{\mathbf{x}}_1(\mathbf{x}_t, t; \theta) - \mathbf{x}_t}{1-t} \quad (10)$$

Since both $\hat{\mathbf{x}}_1(\mathbf{x}_t, t; \theta)$ and $p_t(\mathbf{x}_t|\mathbf{x}_1)$ are easy to sample, we use a single neural network with two separate output heads: the first head, $\hat{\mathbf{x}}_1(\mathbf{x}_t, t; \theta)$, to approximate the data samples, and the second, $\hat{\epsilon}(\mathbf{x}_t, t; \theta)$, to approximate the score function. The network generates these outputs simultaneously. The score function $\nabla_{\mathbf{x}_t} \log p_t(\mathbf{x}_t | \mathbf{x}_1)$, using a Gaussian $p_t(\mathbf{x}_t | \mathbf{x}_1)$, can be simplified to $-\frac{\epsilon_0}{\sigma_t}$, where $\epsilon_0 \sim \mathcal{N}(\mathbf{0}, \mathbf{I})$. The neural network can be trained using the following loss function:

$$\mathcal{L}_{\text{IDFF}}(\theta) = \mathbb{E}_{t, \mathbf{x}_0, \mathbf{x}_1, \mathbf{x}_t} [\beta(t)^2 |\hat{\mathbf{x}}_1(\mathbf{x}_t, t; \theta) - \mathbf{x}_1|^2 + \lambda(t)^2 |\hat{\epsilon}(\mathbf{x}_t, t; \theta) - \nabla_x \log p_t(\mathbf{x}_t|\mathbf{x}_1)|^2] \quad (11)$$

Where $t \sim \mathcal{U}(0, 1)$, $\mathbf{x}_0 \sim \mathcal{N}(\mathbf{0}, \mathbf{I})$, $\mathbf{x}_1 \sim p_{\text{data}}$, $\mathbf{x}_t \sim p_t(\mathbf{x}_t|\mathbf{x}_1)$. Here $\lambda(\cdot), \beta(\cdot)$ are two sets of positive weights.

Our proposed loss function comprises two terms: The first term optimizes the denoising model $\hat{\mathbf{x}}_1(\mathbf{x}_t, t; \theta)$, with \mathbf{x}_t as the noisy input. The second term represents a scoring model that approximates $\nabla_x \log p_t(\mathbf{x}_t|\mathbf{x}_1)$. The first term of the loss incorporates a $\beta(t)$ weighting schedule, which emphasizes the quality of samples as they approach $t = 1$. For more details about the loss function, please refer to Appendix A.1.2. The complete training process is described in Algorithm 1.

Sampling After training $\hat{\mathbf{x}}_1(\cdot; \theta)$ and $\epsilon(\cdot; \theta)$, we can generate samples from IDFF by solving an SDE starting from the source samples \mathbf{x}_0 . Refer to Figure 2.C for visualization. This procedure is outlined in Algorithm 2. The SDE is defined as $d\mathbf{x}_t = \mathbf{w}_t dt + \sigma_t d\mathbf{w}$, with initial samples \mathbf{x}_0 and target samples \mathbf{x}_1 at $t = 1$. Therefore, we can draw samples from $p(\mathbf{x}_0)$, run them through the SDE, and obtain the final samples \mathbf{x}_1 . First, we draw $\mathbf{x}_0 \sim \mathcal{N}(\mathbf{0}, \mathbf{I})$, then compute $\hat{\mathbf{x}}_1(\mathbf{x}_0, 0, k; \theta)$. Next, we calculate $\hat{\mathbf{v}}_t$ using equation 10, followed by the computation of \mathbf{w}_t . After calculating \mathbf{w}_t and using the SDE, we compute the mean for the next time step as $\boldsymbol{\mu}_{t+\Delta t} = (\mathbf{x}_t + \mathbf{w}_t \Delta t)$, and finally draw a sample from a small neighborhood of it: $\mathbf{x}_{t+\Delta t} \sim \mathcal{N}(\mathbf{x}_t + \mathbf{w}_t \Delta t, \sigma_t^2 \Delta t \mathbf{I})$. The Δt is determined by the NFE as $\Delta t = \frac{1}{\text{NFE}}$, where smaller NFE results in finer time discretization and tighter neighborhoods.

Likelihood calculation. To evaluate the likelihood of data under IDFFs, we can leverage the change in the probability density as the sample \mathbf{x}_t evolves according to the velocity field \mathbf{w}_t as described by the continuity equation 4, which gives the time evolution of the probability density under the learned flow Lipman et al. (2022):

$$\log p_1(\mathbf{x}_1) = \log p_0(\mathbf{x}_0) - \int_0^1 \nabla \cdot \mathbf{w}_t(\mathbf{x}_t) dt \quad (12)$$

This integral is numerically approximated, often using Monte Carlo methods.

3.3 IDFF TIME-SERIES ADAPTATION

To use IDFF for time-series applications, we need to modify the training and sampling algorithms for IDFF as shown in Algorithms 4 and 3, respectively. To accomplish that, we define another random variable, k , which is a discrete variable and can take values of $1, \dots, K$ with equal probability, where K is the length of a time series. Therefore, k represents the index of the data sample in a time series. We also have t as a continuous time variable interpolated between two subsequent values of k (i.e., k and $k - 1$). Therefore we have $\forall k \in 1, \dots, K \rightarrow p(t | k) \sim \mathcal{U}(0, 1)$. This conditioning does not change the original assumption over t since k can take any values up to the time-series length with the same probability. With this in hand, we can directly pass the k as additional inputs to $\hat{\epsilon}_1(\mathbf{x}_t, t, k; \theta)$ and $\hat{\mathbf{x}}_1(\mathbf{x}_t, t, k; \theta)$ and suggest Algorithm 1 for training and Algorithm 2 for sampling time-series data with IDFF. Note that for static data, the sequence length (K) equals one; otherwise, it equals the time series length.

4 RELATED WORK

Recent advancements in CFMs include Schrödinger bridge-based methods (Richter et al., 2023) and conjugate/splitting-based integrators (Pandey et al., 2023), both aimed at improving sampling efficiency. However, these methods still struggle to significantly reduce the NFEs, which remains a critical factor for computational efficiency.

In diffusion models, denoising diffusion implicit models (DDIMs) (Song et al., 2020b) were introduced to address the issue of large NFEs by offering a more efficient sampling process. DDIMs deterministically generate samples from latent variables, unlike DDPMs, which rely on Langevin dynamics. By employing a variational approach, DDIMs accelerate sampling while preserving output quality. Other approaches to enhance sampling in diffusion-based generative models include distillation frameworks such as Flash (Kohler et al., 2024), which generate diverse samples in fewer steps by mitigating training-inference discrepancies.

A distinguishing feature of IDFF is its ability to jointly learn an implicit flow from the generated samples alongside the scoring model. This sets it apart from models like DDIM, which focuses solely

378
379
380
381
382
383
384
385
386
387
388
389
390
391
392
393
394

Algorithm 1 IDFF training algorithm.

Input: dataset distribution $p_1(\mathbf{x}_1)$, initial distribution $p_0(\mathbf{x}_0)$, bandwidth σ_0 , a set of positive weights $\lambda(\cdot)$ and $\beta(\cdot)$, initialized networks $\hat{\mathbf{x}}_1(\cdot; \theta)$ and $\hat{\epsilon}(\cdot; \theta)$,
while Training **do**
 $\mathbf{x}_1 \sim p_1(\mathbf{x}_1)$, $\mathbf{x}_0 \sim p_0(\mathbf{x}_0)$
 $\pi \leftarrow \text{OT}(\mathbf{x}_1, \mathbf{x}_0)$
 $(\mathbf{x}_0, \mathbf{x}_1) \sim \pi$
 $t \sim \mathcal{U}(0, 1)$
 $\boldsymbol{\mu}_t \leftarrow t\mathbf{x}_1 + (1-t)\mathbf{x}_0$
 $\sigma_t \leftarrow \sigma_0\sqrt{t(1-t)}$
 $\mathbf{x}_t \sim \mathcal{N}(\boldsymbol{\mu}_t, \sigma_t^2\mathbf{I})$
 $\mathcal{L}_{\text{IDFF}}(\theta) \leftarrow \beta(t)^2 \|\hat{\mathbf{x}}_1(\mathbf{x}_t, t, k; \theta) - \mathbf{x}_1\|^2 + \lambda(t)^2 \|\epsilon(\mathbf{x}_t, t; \theta) - \nabla_x \log p_t(\mathbf{x}_t|\mathbf{x}_1)\|^2$
 $\theta \leftarrow \text{Update}(\theta, \nabla_{\theta} L(\theta))$
end while
return $\{\hat{\mathbf{x}}_1(\cdot; \theta), \hat{\epsilon}(\cdot; \theta)\}$

Algorithm 2 IDFF Sampling algorithm

Input: $\hat{\mathbf{x}}_1(\cdot; \theta)$ and $\hat{\epsilon}(\cdot; \theta)$, bandwidth σ_0 , time step size Δt , and γ .
 $\mathbf{x}_0^0 \sim \mathcal{N}(0, \mathbf{I})$
for t in $[0, 1/\Delta t)$ **do**
 $\sigma_t \leftarrow \sigma_0\sqrt{t(1-t)}$
 $\mathbf{w}_t \leftarrow \sqrt{(1-\sigma_t^2)} \frac{\hat{\mathbf{x}}_1(\mathbf{x}_t, t; \theta) - \mathbf{x}_t}{1-t} + \frac{2\gamma-1}{2} \sigma_t \hat{\epsilon}(\mathbf{x}_t, t; \theta)$
 $\mathbf{x}_{t+\Delta t} \sim \mathcal{N}(\mathbf{x}_t + \mathbf{w}_t \Delta t, \sigma_t^2 \Delta t \mathbf{I})$
end for
return Samples $\{\mathbf{x}_1\}$

395 on learning a scoring function. By leveraging OT to couple samples between $t = 0$ and $t = 1$, IDFF
396 accelerates convergence during training while maintaining a low NFE and improving sample quality.

397 Our image generation experiments, presented in Tables 1 and 2, demonstrate IDFF’s superior
398 performance. Compared to $[SF]^2M$ (Tong et al., 2023b), OT-CFM(Pooladian et al., 2023), DDPM
399 (Ho et al., 2020), DDIM (Song et al., 2020b), EDM (Karras et al., 2022), and DPM-Solver (Lu et al.,
400 2022a) (designed to reduce NFEs in diffusion models), IDFF consistently outperforms these models
401 in both efficiency and quality.

402 In summary, IDFF combines conditional flow and
403 score-based learning, providing an efficient frame-
404 work for generative modeling that reduces computa-
405 tional costs while achieving high-quality samples in
406 training iterations, much fewer than diffusion-based
407 models and comparable to CFM (see Appendix A.3
408 for details). The next section elaborates on these
409 comparisons.

411 5 EXPERIMENTS

412 We conducted two general classes of experiments to
413 demonstrate the effectiveness of IDFF in generative
414 modeling on static data, such as images and time-
415 series data, including simulated chaotic systems (e.g.,
416 attractors), molecular dynamics, and sea surface tem-
417 perature forecasting. The anonymous code for our
418 implementation is accessible at Anonymous Repository.

421 5.1 IMAGE GENERATION

422 *IDFFs exhibit superior performance compared*
423 *to CFMs in image generation.* We trained
424 IDFF models on datasets such as CIFAR-10
425 and CelebA (additional results for ImageNet-
426 64, CelebA-HQ, LSUN Bedrooms, and LSUN
427 Church are available in Appendix A.6). We uti-
428 lized a CNN-based UNet (Dhariwal and Nichol,
429 2021) to simultaneously model both $\hat{\mathbf{x}}_1(\cdot, t; \theta)$
430 and $\epsilon(\cdot, t; \theta)$ from Equation 11 for all image data
431 except ImageNet-64. For ImageNet-64, we em-
432 ployed a DiT architecture (‘DiT-L/4’)(Peebles

Table 1: Comparison of Likelihood (BPD), FID, and NFE between IDFF and various methods on the CIFAR-10 dataset. Additional results are provided in Table 7

Model	NLL↓	FID↓	NFE↓
DDPM	3.12	7.48	274
EDM	–	16.57	10
DDIM	–	6.84	20
DDIM	–	13.36	10
DPM-Solver	–	6.03	12
Score Matching	3.16	19.94	242
ScoreFlow	3.09	20.78	428
OT-CFM	2.99	6.35	142
OT-CFM	–	11.87	10
$[SF]^2M$	–	10.13	10
FM	–	14.36	10
IC-CFM	–	13.68	10
IDFF (Ours)	3.09	5.87	10

Table 2: Comparison of FID and NFE metrics between IDFF and various methods on the CelebA (64 × 64) dataset.

Model	FID↓	NFE↓
DDPM	45.20	100
DDIM	13.73	20
DDIM	17.33	10
FastDPM	12.83	50
IDFF (Ours)	11.83	10

and Xie, 2022). To implement this, we doubled the input channels of the networks and fed the augmented input, $(\mathbf{x}_t, \mathbf{x}_t)$, into the network. The outputs were then split into $(\hat{\mathbf{x}}_1(\cdot, t; \theta), \epsilon(\cdot, t; \theta))$.

To ensure a fair comparison with other models, we used commonly employed metrics to evaluate CFMs’ performance, including negative log-likelihood (NLL) using equation 12 measured in bits per dimension (BPD) Lipman et al. (2022), sample quality as measured by the Frechet Inception Distance (FID), and the average NFE required for the reported FID and NLL, averaged over 50k samples, to assess the computational efficiency of our method. We generate 50k images to calculate the FID against the corresponding reference statistics of each dataset. All models use the same architecture, with specific details provided in Appendix A.5.

We also examined the effect of σ_0 on sample quality for both CIFAR-10 and CelebA datasets in Appendix A.2, finding that a value of $\sigma_0 = 0.6$ achieved the best FID for both datasets, as shown in Table 1 and Table 2. IDFF achieves comparable FID scores with ten times fewer NFEs than CFM and DDPM on the CIFAR-10 and CelebA datasets. IDFF’s qualitative results are provided in Figure 1 (additional samples are available in Appendix A.6).

Figure 4 (A) displays the FID score for the initial 50k generated samples plotted against NFEs for both the CIFAR-10 and CelebA datasets. Sample quality improves rapidly when the NFE exceeds 4, highlighting the significantly lower sampling cost of IDFF compared to traditional CFMs and diffusion-based models.

5.2 TIME SERIES GENERATION

To assess the performance of IDFF in modeling time series data, we evaluated IDFF on three distinct tasks: 3D-attractor generation (see Appendix A.7), molecular dynamics simulation, and sea surface temperature forecasting.

5.2.1 MOLECULAR DYNAMICS SIMULATION

IDFFs can predict dynamics for complex combinatorial structures such as molecules. Molecular dynamics simulation is a crucial tool in quantum mechanics for understanding the dynamics of molecular behavior at the atomic level (Cazorla and Boronat, 2017). Here, we simulated a fully extended polyaniline structure for 400 picoseconds in a vacuum environment at a temperature of $T = 300K$. This molecular structure consists of 253 atoms with 46 dihedral angles. We trained an IDFF model to accurately generate the dihedral angles for the polyaniline structure from scratch. The distributions of the actual and generated dihedral angles for all 46 angles are presented in Figure 3 (A) and (B), respectively. Figure 3 (C) illustrates the dihedral angles for one of the alanine molecules and its associated dihedral angles. A complete trajectory showcasing a pair of actual and generated dihedral angles is depicted in Figure 3 (D).

To assess the performance of IDFF in the MD simulation, we utilized several evaluation metrics, including root mean squared error (RMSE), mean absolute error (MAE), and correlation coefficients (CC) between the generated and actual trajectories of dihedral angles. We benchmarked IDFF against well-known dynamical models for time series, including dynamical VAE models such as SRNNs (Fraccaro et al., 2016), VRNNs (Chung et al., 2015), and Neural ODEs (NODEs) (Garnelo et al., 2018). As shown in Table 3, IDFF outperforms the baselines by a large margin, indicating its potential for simulating molecular dynamics from scratch.

5.2.2 SEA SURFACE TEMPERATURE FORECASTING

IDFFs can predict spatiotemporal dynamics for sea-surface temperature. This experiment centers on forecasting sea surface temperature (SST) (Worsfold et al., 2024). Using the NOAA OISSTv2 dataset, which contains daily high-resolution SST images spanning from 1982 to 2021 (Cachay et al.,

Table 3: MAE, RMSE, and CC between true and predicted trajectories for the MD simulation.

Method	MAE↓	RMSE↓	CC (%)↑
SRNN	82.6±28	91.9±25	10.2±0.27
DVAE	78.1±27	88.1±25	30.4±0.35
NODE	25.3±6.3	28.8±6.2	10.5±0.41
OT-CFM			
NFE=50	13.3±1.1	16.3±2.4	86.1±0.1
NFE=10	15.5±1.3	19.2±2.7	82.4±0.2
IDFF			
NFE=5	10.3±1.3	14.9±2.7	93.2±0.05
NFE=12	9.5±1.1	13.4±2.8	95.2±0.1

2023), we partitioned the data to predict SST intervals from 1 to 7 days ahead. To achieve this, we strategically subsampled eleven grid tiles of size 60×60 (latitude \times longitude) from the eastern tropical Pacific region (Huang et al., 2021).

We used a class-conditional UNet for the SST experiment, with the class encoder part encoding the long-range time dependencies (i.e., for encoding the days) to allow continuous forecasting using the UNet. See Appendix A.5 for the experiment’s network structure and hyperparameter settings. We used the training 4 and sampling 3 algorithms suggested for time-series data. We evaluated the performance of IDFF using the best validation continuous ranked probability score (CRPS) (Matheson and Winkler, 1976) and mean squared error (MSE) on forecasts up to 7 days. CRPS is a proper scoring rule and a popular metric in probabilistic forecasting literature (Gneiting and Katzfuss, 2014). We calculate the CRPS by generating a 20-member ensemble and the MSE on the ensemble mean predictions in Table 4.

To assess IDFF’s performance, we compared it against various baseline approaches, including DDPM, DDPM with enabled dropout (Dropout) (Gal and Ghahramani, 2016), DDPM with random perturbation for the initial values (Perturbation) (Pathak et al., 2022), MCVD (Voleti et al., 2022), Dyffusion (Cachay et al., 2023), and OT-CFM (with $NFE = 40$) as shown in Table 4. The results for all the baselines are with $NFE = 1000$. These baselines provide a robust framework for evaluating the IDFF framework in time-series forecasting. The results show that IDFF (with $NFE = 5$) outperforms the baselines in SST forecasting across both metrics, demonstrating great potential for weather forecasting applications. See samples of the forecasting results in Figure 14.

6 CONCLUSION AND DISCUSSION

IDFF models represent a significant advancement in generative modeling, particularly for time series data. By offering superior computational efficiency compared to traditional flow models like CFMs, IDFF achieves a favorable balance between computational cost and sample quality. This makes IDFF a compelling choice for tasks requiring efficient and high-quality sample generation. There are myriad future possibilities for the application of IDFF in domains such as music generation (Briot et al., 2017), speech synthesis (Yu and Deng, 2016), and modeling biological time-series data (Anumanchipalli et al., 2019; Golshan et al., 2020; Rezaei et al., 2021; 2023; Gracco et al., 2005).

Limitations and Future Work: Computing the OT map for large datasets can be challenging. To address this, we use a minibatch approximation of OT; however, increasing the batch size results in longer training times for larger batches. Second, our experiments primarily utilized a CNN-based UNet structure (Dhariwal and Nichol, 2021) as the backbone of the models. We anticipate that some of these limitations may be mitigated by utilizing new neural network structures (Peebles and Xie, 2023).

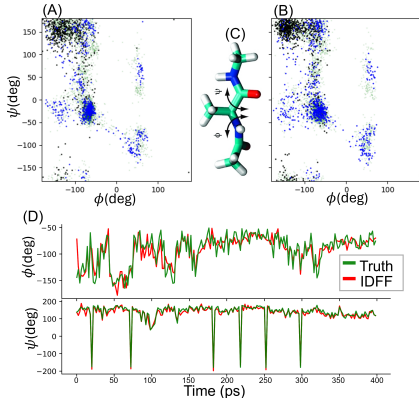


Figure 3: (A) True and (B) generated dihedral angles. (C) The dihedral angles for an alanine molecule. (D) True and generated dihedral angle trajectories using IDFF.

Table 4: Results for sea surface temperature forecasting of 1 to 7 days ahead, averaged over the evaluation horizon.

Method	CRPS \downarrow	MSE \downarrow
Perturb.	0.281 ± 0.004	0.180 ± 0.011
Dropout	0.267 ± 0.003	0.164 ± 0.004
DDPM	0.246 ± 0.005	0.177 ± 0.005
MCVD	0.216	0.161
Dyffusion	0.224 ± 0.001	0.173 ± 0.001
OT-CFM	0.231 ± 0.005	0.175 ± 0.006
IDFF (Ours)	0.180 ± 0.024	0.105 ± 0.029

REFERENCES

- 540
541
542 Salva Rühling Cachay, Bo Zhao, Hailey James, and Rose Yu. Dyffusion: A dynamics-informed
543 diffusion model for spatiotemporal forecasting. *arXiv preprint arXiv:2306.01984*, 2023.
- 544
545 Catherine E Myers, Alejandro Interian, and Ahmed A Moustafa. A practical introduction to using
546 the drift diffusion model of decision-making in cognitive psychology, neuroscience, and health
547 sciences. *Frontiers in Psychology*, 13:1039172, 2022.
- 548
549 Yang Song, Jascha Sohl-Dickstein, Diederik P Kingma, Abhishek Kumar, Stefano Ermon, and Ben
550 Poole. Score-based generative modeling through stochastic differential equations. *arXiv preprint*
551 *arXiv:2011.13456*, 2020a.
- 552
553 Yixin Liu, Kai Zhang, Yuan Li, Zhiling Yan, Chujie Gao, Ruoxi Chen, Zhengqing Yuan, Yue Huang,
554 Hanchi Sun, Jianfeng Gao, et al. Sora: A review on background, technology, limitations, and
555 opportunities of large vision models. *arXiv preprint arXiv:2402.17177*, 2024.
- 556
557 Dong Wook Kim, Hye Young Jang, Kyung Won Kim, Youngbin Shin, and Seong Ho Park. De-
558 sign characteristics of studies reporting the performance of artificial intelligence algorithms for
559 diagnostic analysis of medical images: results from recently published papers. *Korean journal of*
560 *radiology*, 20(3):405–410, 2019.
- 561
562 Jonathan Ho, Ajay Jain, and Pieter Abbeel. Denoising diffusion probabilistic models. *Advances in*
563 *Neural Information Processing Systems*, 33:6840–6851, 2020.
- 564
565 Cheng Lu, Yuhao Zhou, Fan Bao, Jianfei Chen, Chongxuan Li, and Jun Zhu. Dpm-solver: A fast
566 ode solver for diffusion probabilistic model sampling in around 10 steps. *Advances in Neural*
567 *Information Processing Systems*, 35:5775–5787, 2022a.
- 568
569 Cheng Lu, Yuhao Zhou, Fan Bao, Jianfei Chen, Chongxuan Li, and Jun Zhu. Dpm-solver++: Fast
570 solver for guided sampling of diffusion probabilistic models. *arXiv preprint arXiv:2211.01095*,
571 2022b.
- 572
573 Jiaming Song, Chenlin Meng, and Stefano Ermon. Denoising diffusion implicit models. *arXiv*
574 *preprint arXiv:2010.02502*, 2020b.
- 575
576 Xingchao Liu, Chengyue Gong, and Qiang Liu. Flow straight and fast: Learning to generate and
577 transfer data with rectified flow. *arXiv preprint arXiv:2209.03003*, 2022.
- 578
579 Michael S Albergo and Eric Vanden-Eijnden. Building normalizing flows with stochastic interpolants.
580 *arXiv preprint arXiv:2209.15571*, 2022.
- 581
582 Michael S Albergo, Nicholas M Boffi, and Eric Vanden-Eijnden. Stochastic interpolants: A unifying
583 framework for flows and diffusions. *arXiv preprint arXiv:2303.08797*, 2023.
- 584
585 Yaron Lipman, Ricky TQ Chen, Heli Ben-Hamu, Maximilian Nickel, and Matt Le. Flow matching
586 for generative modeling. *arXiv preprint arXiv:2210.02747*, 2022.
- 587
588 Quan Dao, Hao Phung, Binh Nguyen, and Anh Tran. Flow matching in latent space. *arXiv preprint*
589 *arXiv:2307.08698*, 2023.
- 590
591 Radford M Neal. *Bayesian learning for neural networks*, volume 118. Springer Science & Business
592 Media, 2012a.
- 593
594 Radford M Neal et al. Mcmc using hamiltonian dynamics. *Handbook of markov chain monte carlo*,
2(11):2, 2011.
- 595
596 Yang Song and Stefano Ermon. Generative modeling by estimating gradients of the data distribution.
597 *Advances in neural information processing systems*, 32, 2019.
- 598
599 Alexander Tong, Nikolay Malkin, Guillaume Hugué, Yanlei Zhang, Jarrid Rector-Brooks, Kilian
600 Fatras, Guy Wolf, and Yoshua Bengio. Improving and generalizing flow-based generative models
601 with minibatch optimal transport. *arXiv preprint arXiv:2302.00482*, 2023a.

- 594 Alexander Tong, Nikolay Malkin, Kilian Fatras, Lazar Atanackovic, Yanlei Zhang, Guillaume Hugué,
595 Guy Wolf, and Yoshua Bengio. Simulation-free Schrödinger bridges via score and flow matching.
596 *arXiv preprint arXiv:2307.03672*, 2023b.
- 597
598 Alexander Tong, Jessie Huang, Guy Wolf, David Van Dijk, and Smita Krishnaswamy. TrajectoryNet:
599 A dynamic optimal transport network for modeling cellular dynamics. In *International conference*
600 *on machine learning*, pages 9526–9536. PMLR, 2020.
- 601
602 Aram-Alexandre Pooladian, Heli Ben-Hamu, Carles Domingo-Enrich, Brandon Amos, Yaron Lipman,
603 and Ricky Chen. Multisample flow matching: Straightening flows with minibatch couplings. *arXiv*
604 *preprint arXiv:2304.14772*, 2023.
- 605
606 Radford M Neal. MCMC using hamiltonian dynamics. *arXiv preprint arXiv:1206.1901*, 2012b.
- 607
608 Kilian Fatras, Thibault Séjourné, Rémi Flamary, and Nicolas Courty. Unbalanced minibatch optimal
609 transport; applications to domain adaptation. In *International Conference on Machine Learning*,
610 pages 3186–3197. PMLR, 2021.
- 611
612 Aude Genevay, Gabriel Peyré, and Marco Cuturi. Learning generative models with sinkhorn diver-
613 gences. In *International Conference on Artificial Intelligence and Statistics*, pages 1608–1617.
614 PMLR, 2018.
- 615
616 Lorenz Richter, Julius Berner, and Guan-Hong Liu. Improved sampling via learned diffusions. *arXiv*
617 *preprint arXiv:2307.01198*, 2023.
- 618
619 Kushagra Pandey, Maja Rudolph, and Stephan Mandt. Efficient integrators for diffusion generative
620 models. *arXiv preprint arXiv:2310.07894*, 2023.
- 621
622 Jonas Kohler, Albert Pumarola, Edgar Schönfeld, Artsiom Sanakoyeu, Roshan Sumbaly, Peter Vajda,
623 and Ali Thabet. Imagine flash: Accelerating emu diffusion models with backward distillation.
624 *arXiv preprint arXiv:2405.05224*, 2024.
- 625
626 Tero Karras, Miika Aittala, Timo Aila, and Samuli Laine. Elucidating the design space of diffusion-
627 based generative models. *Advances in neural information processing systems*, 35:26565–26577,
628 2022.
- 629
630 Prafulla Dhariwal and Alexander Nichol. Diffusion models beat GANs on image synthesis. *Advances*
631 *in neural information processing systems*, 34:8780–8794, 2021.
- 632
633 W Peebles and S Xie. Scalable diffusion models with transformers. arXiv e-prints, art. *arXiv preprint*
634 *arXiv:2212.09748*, 2022.
- 635
636 Claudio Cazorla and Jordi Boronat. Simulation and understanding of atomic and molecular quantum
637 crystals. *Reviews of Modern Physics*, 89(3):035003, 2017.
- 638
639 Marco Fraccaro, Søren Kaae Sønderby, Ulrich Paquet, and Ole Winther. Sequential neural models
640 with stochastic layers. *Advances in neural information processing systems*, 29, 2016.
- 641
642 Junyoung Chung, Kyle Kastner, Laurent Dinh, Kratarth Goel, Aaron C Courville, and Yoshua Bengio.
643 A recurrent latent variable model for sequential data. *Advances in neural information processing*
644 *systems*, 28, 2015.
- 645
646 Marta Garnelo, Jonathan Schwarz, Dan Rosenbaum, Fabio Viola, Danilo J Rezende, SM Eslami, and
647 Yee Whye Teh. Neural processes. *arXiv preprint arXiv:1807.01622*, 2018.
- 648
649 Mark Worsfold, Simon Good, Chris Atkinson, and Owen Embury. Presenting a long-term, reprocessed
650 dataset of global sea surface temperature produced using the OSTIA system. *Remote Sensing*, 16
651 (18), 2024. ISSN 2072-4292. doi: 10.3390/rs16183358. URL [https://www.mdpi.com/](https://www.mdpi.com/2072-4292/16/18/3358)
652 [2072-4292/16/18/3358](https://www.mdpi.com/2072-4292/16/18/3358).
- 653
654 Boyin Huang, Chunying Liu, Viva Banzon, Eric Freeman, Garrett Graham, Bill Hankins, Tom Smith,
655 and Huai-Min Zhang. Improvements of the daily optimum interpolation sea surface temperature
656 (DOISST) version 2.1. *Journal of Climate*, 34(8):2923–2939, 2021.

- 648 James E Matheson and Robert L Winkler. Scoring rules for continuous probability distributions.
649 *Management science*, 22(10):1087–1096, 1976.
- 650
- 651 Tilmann Gneiting and Matthias Katzfuss. Probabilistic forecasting. *Annual Review of Statistics and*
652 *Its Application*, 1:125–151, 2014.
- 653 Yarin Gal and Zoubin Ghahramani. Dropout as a bayesian approximation: Representing model
654 uncertainty in deep learning. In *international conference on machine learning*, pages 1050–1059.
655 PMLR, 2016.
- 656
- 657 Jaideep Pathak, Shashank Subramanian, Peter Harrington, Sanjeev Raja, Ashesh Chattopadhyay,
658 Morteza Mardani, Thorsten Kurth, David Hall, Zongyi Li, Kamyar Azizzadenesheli, et al. Fourcast-
659 net: A global data-driven high-resolution weather model using adaptive fourier neural operators.
660 *arXiv preprint arXiv:2202.11214*, 2022.
- 661 Vikram Voleti, Alexia Jolicoeur-Martineau, and Chris Pal. Mcvd-masked conditional video diffusion
662 for prediction, generation, and interpolation. *Advances in Neural Information Processing Systems*,
663 35:23371–23385, 2022.
- 664 Jean-Pierre Briot, Gaëtan Hadjeres, and François-David Pachet. Deep learning techniques for music
665 generation—a survey. *arXiv preprint arXiv:1709.01620*, 2017.
- 666
- 667 Dong Yu and Li Deng. *Automatic speech recognition*, volume 1. Springer, 2016.
- 668
- 669 Gopala K Anumanchipalli, Josh Chartier, and Edward F Chang. Speech synthesis from neural
670 decoding of spoken sentences. *Nature*, 568(7753):493–498, 2019.
- 671 Hosein M Golshan, Adam O Hebb, and Mohammad H Mahoor. Lfp-net: A deep learning framework
672 to recognize human behavioral activities using brain stn-lfp signals. *Journal of neuroscience*
673 *methods*, 335:108621, 2020.
- 674
- 675 Mohammad Reza Rezaei, Kensuke Arai, Loren M Frank, Uri T Eden, and Ali Yousefi. Real-time
676 point process filter for multidimensional decoding problems using mixture models. *Journal of*
677 *neuroscience methods*, 348:109006, 2021.
- 678
- 679 Mohammad R Rezaei, Haseul Jeoung, Ayda Gharamani, Utpal Saha, Venkat Bhat, Milos R Popovic,
680 Ali Yousefi, Robert Chen, and Milad Lankarany. Inferring cognitive state underlying conflict
681 choices in verbal stroop task using heterogeneous input discriminative-generative decoder model.
Journal of Neural Engineering, 20(5):056016, 2023.
- 682
- 683 Vincent L Gracco, Pascale Tremblay, and Bruce Pike. Imaging speech production using fmri.
684 *Neuroimage*, 26(1):294–301, 2005.
- 685
- 686 William Peebles and Saining Xie. Scalable diffusion models with transformers. In *Proceedings of*
687 *the IEEE/CVF International Conference on Computer Vision*, pages 4195–4205, 2023.
- 688
- 689 Alexia Jolicoeur-Martineau, Rémi Piché-Taillefer, Rémi Tachet des Combes, and Ioannis Mitliagkas.
690 Adversarial score matching and improved sampling for image generation. *arXiv preprint*
691 *arXiv:2009.05475*, 2020.
- 692
- 693 Ajay Jain, Pieter Abbeel, and Deepak Pathak. Locally masked convolution for autoregressive models.
694 In *Conference on Uncertainty in Artificial Intelligence*, pages 1358–1367. PMLR, 2020.
- 695
- 696 Wenliang Zhao, Lujia Bai, Yongming Rao, Jie Zhou, and Jiwen Lu. Unipc: A unified predictor-
697 corrector framework for fast sampling of diffusion models. *Advances in Neural Information*
698 *Processing Systems*, 36, 2024.
- 699
- 700
- 701 Kaiwen Zheng, Cheng Lu, Jianfei Chen, and Jun Zhu. Dpm-solver-v3: Improved diffusion ode
solver with empirical model statistics. *Advances in Neural Information Processing Systems*, 36:
55502–55542, 2023.

701 A APPENDIX

702	CONTENTS	
703		
704	1 Introduction	1
705		
706	2 Background	2
707		
708		
709	3 Implicit Dynamical Flow Fusion Model (IDFF)	5
710	3.1 Learning CFMs with Momentum	5
711	3.2 Learning Flows in Input Space	6
712	3.3 IDFF time-series adaptation	7
713		
714		
715	4 Related Work	7
716		
717		
718	5 Experiments	8
719	5.1 Image Generation	8
720	5.2 Time Series Generation	9
721	5.2.1 Molecular Dynamics Simulation	9
722	5.2.2 Sea Surface Temperature Forecasting	9
723		
724		
725		
726	6 Conclusion and Discussion	10
727		
728	A Appendix	13
729	A.1 Proofs	15
730	A.1.1 Continuity proof for Lemma 1	15
731	A.1.2 Training objective derivations	15
732	A.2 Balancing the IDFF flow	16
733	A.3 On Convergence Speed of IDFF	16
734	A.4 IDFF training and sampling algorithms for time series	18
735	A.5 Implementation details	18
736	A.6 Additional results for image generation experiment	19
737	A.7 3D-attractors	20
738	A.8 SST forecasting visualization	21
739	A.9 2D-simulated static data and time-series	21
740		
741		
742		
743		
744		
745		
746		
747		
748		
749		
750		
751		
752		
753		
754		
755		

756 A.1 PROOFS

757 A.1.1 CONTINUITY PROOF FOR LEMMA 1

758 We define a vector field as follows:

759
760
761
762
$$\tilde{\mathbf{v}}_t(\mathbf{x}_t) = \sqrt{1 - \sigma_t^2} \mathbf{v}_t(\mathbf{x}_t) + \sigma_t^2 \boldsymbol{\xi}_t, \quad \boldsymbol{\xi}_t = \gamma \nabla \log p_t(\mathbf{x}_t) \quad (13)$$

763 where γ is a coefficient controlling the contribution of the momentum term $\boldsymbol{\xi}_t$.

764 Consider a Stochastic Differential Equation (SDE) of the standard form:

765
766
767
$$d\mathbf{x}_t = \tilde{\mathbf{v}}_t(\mathbf{x}_t) dt + \sigma_t d\mathbf{w} \quad (14)$$

768 with time parameter t , drift $\tilde{\mathbf{v}}_t$, diffusion coefficient σ_t , and $d\mathbf{w}$ representing the Wiener process.

769 The solution \mathbf{x}_t to the SDE is a stochastic process with probability density $p_t(\mathbf{x}_t)$, characterized by the Fokker-Planck equation:

770
771
772
$$\frac{\partial p_t(\mathbf{x}_t)}{\partial t} = -\nabla \cdot (\tilde{\mathbf{v}}_t(\mathbf{x}_t) p_t(\mathbf{x}_t)) + \frac{\sigma_t^2}{2} \Delta p_t(\mathbf{x}_t) \quad (15)$$

773 where Δ represents the Laplace operator in \mathbf{x}_t .

774 We can rewrite this equation in the form of the continuity equation:

775
776
777
$$\frac{\partial p_t(\mathbf{x}_t)}{\partial t} = -\nabla \cdot \left(\tilde{\mathbf{v}}_t(\mathbf{x}_t) p_t(\mathbf{x}_t) - \frac{\sigma_t^2}{2} \frac{\nabla p_t(\mathbf{x}_t)}{p_t(\mathbf{x}_t)} p_t(\mathbf{x}_t) \right) \quad (16)$$

781
782
$$= -\nabla \cdot \left(\left(\tilde{\mathbf{v}}_t(\mathbf{x}_t) - \frac{\sigma_t^2}{2} \nabla \log p_t(\mathbf{x}_t) \right) p_t(\mathbf{x}_t) \right) \quad (17)$$

783
784
785
$$= -\nabla \cdot (\mathbf{w}_t p_t(\mathbf{x}_t)) \quad (18)$$

786 where the vector field \mathbf{w}_t is defined as:

787
788
789
$$\mathbf{w}_t(\mathbf{x}_t) = \tilde{\mathbf{v}}_t(\mathbf{x}_t) - \frac{\sigma_t^2}{2} \nabla \log p_t(\mathbf{x}_t) = \sqrt{1 - \sigma_t^2} \mathbf{v}_t(\mathbf{x}_t) + \frac{2\gamma - 1}{2} \sigma_t^2 \nabla \log p_t(\mathbf{x}_t) \quad (19)$$

790 As t approaches 0 or 1, $\sigma_t \rightarrow 0$, causing $\tilde{\mathbf{v}}_t(\mathbf{x}_t)$ to converge to $\hat{\mathbf{v}}_t(\mathbf{x}_t)$. This ensures that the continuity equation is satisfied with the probability path $p_t(\mathbf{x}_t)$ for the original equation.

791
792
793
794
795 A.1.2 TRAINING OBJECTIVE DERIVATIONS

796 As described in Theorem 2 of (Lipman et al., 2022), the FM loss is defined as:

797
798
$$\mathcal{L}_{\text{FM}}(\theta) = \mathbb{E}_{t, \mathbf{x}_1, p_t(\mathbf{x}_t | \mathbf{x}_1)} \left\| \mathbf{v}_t(\mathbf{x}_t) - \hat{\mathbf{v}}_t(\mathbf{x}_t) \right\|^2 \quad (20)$$

799 The CFM loss, as defined in equation 5, is equivalent to the FM loss up to a constant value, implying that $\mathcal{L}_{\text{FM}}(\theta) = \mathcal{L}_{\text{CFM}}(\theta)$. Based on this equivalence, we can express the training objective for approximating the vector field in equation 7, $\hat{f}_t(\mathbf{x}_t, t | \mathbf{x}_1, \mathbf{x}_0; \theta)$, as:

800
801
$$\mathcal{L}_{\text{IDFF}}^1(\theta) = \mathbb{E}_{t, \mathbf{x}_1, p_t(\mathbf{x}_t | \mathbf{x}_1)} \left\| \hat{\mathbf{v}}_t(\mathbf{x}_t | \mathbf{x}_1; \theta) - \mathbf{v}_t(\mathbf{x}_t | \mathbf{x}_1) \right\|^2 \quad (21)$$

802 To recover unbiased samples, we replace $\hat{u}(\cdot)$ with equation 10 and $\hat{\mathbf{v}}_t(\mathbf{x}_t | \mathbf{x}_1, \mathbf{x}_0)$ with equation 9, resulting in:

803
804
805
$$\mathcal{L}_{\text{IDFF}}^1(\theta) = \mathbb{E}_{t, \mathbf{x}_1, p_t(\mathbf{x}_t | \mathbf{x}_1)} \left[\left\| \frac{\hat{\mathbf{x}}_1(\mathbf{x}_t, t; \theta) - \mathbf{x}_t}{1 - t} - \frac{\mathbf{x}_1 - \mathbf{x}_t}{1 - t} \right\|^2 \right] \quad (22)$$

806
807
$$= \mathbb{E}_{t, \mathbf{x}_1, p_t(\mathbf{x}_t | \mathbf{x}_1)} \left[\beta(t)^2 \left\| \hat{\mathbf{x}}_1(\mathbf{x}_t, t; \theta) - \mathbf{x}_1 \right\|^2 \right] \quad (23)$$

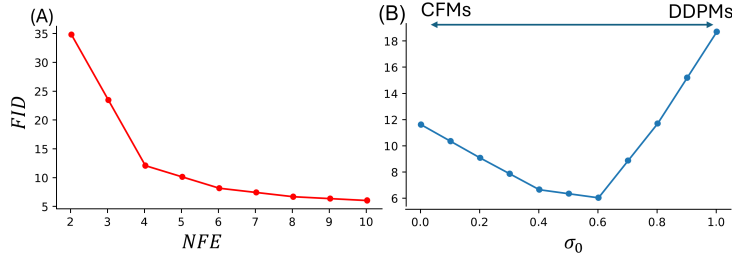


Figure 4: IDFF performance against A) the number of function evaluations (NFEs) and B) the hyperparameter σ_0 (the flow and score model mixing term) with fixed NFE=10 for the CIFAR-10 dataset. Similar analysis for CelebA-64 is shown in Figure 5

where $\beta(t) = \frac{1}{1-t}$. Therefore, we have:

$$\mathcal{L}_{\text{IDFF}}^1(\theta) = \mathbb{E}_{t, \mathbf{x}_1, p_t(\mathbf{x}_t | \mathbf{x}_1)} [\beta(t)^2 \|\hat{\mathbf{x}}_1(\mathbf{x}_t, t; \theta) - \mathbf{x}_1\|^2] \quad (24)$$

To approximate $\nabla_{\mathbf{x}} \log p_t(\mathbf{x}_t | \mathbf{x}_1)$, we can employ a time-dependent score-based model, $\epsilon(\mathbf{x}_t, t; \theta)$, using a continuous loss function with a weighting schedule $\lambda(t)$. Since $\nabla_{\mathbf{x}} \log p_t(\mathbf{x}_t | \mathbf{x}_1)$ approaches infinity as t tends to 0 or 1, it is necessary to standardize the loss to maintain consistency over time. We set $\lambda(t)$ such that the target has zero mean and unit variance, predicting the noise added in sampling \mathbf{x}_t before multiplying by $\sigma_t = \sigma_0 \sqrt{t(1-t)}$. This leads to $\lambda(t) = \sigma_t = \sigma_0 \sqrt{t(1-t)}$, ensuring that the regression target for $\hat{\epsilon}$ is distributed as $\mathcal{N}(\mathbf{0}, \mathbf{I})$. Notably, this loss function is independent of the γ value, allowing us to use the same model with different γ values during the sampling process without altering the minima. The loss is defined as:

$$\mathcal{L}_{\text{IDFF}}^2(\theta) = \mathbb{E}_{t, \mathbf{x}_1, p_t(\mathbf{x}_t | \mathbf{x}_1)} [\lambda(t)^2 \|\hat{\epsilon}(\mathbf{x}_t, t; \theta) - \nabla_{\mathbf{x}} \log p_t(\mathbf{x}_t | \mathbf{x}_1)\|^2] \quad (25)$$

where $\lambda(\cdot)$ is a set of positive weights. With a proper choice of $\lambda(t)$, this loss is equivalent to the original DDPM loss up to a constant value, according to Theorem 1 of (Song et al., 2020b). Combining the two components, the IDFF loss function is defined as:

$$\mathcal{L}_{\text{IDFF}}(\theta) = \mathcal{L}_{\text{IDFF}}^1(\theta) + \mathcal{L}_{\text{IDFF}}^2(\theta) \quad (26)$$

Which leads to the final objective function:

$$\mathcal{L}_{\text{IDFF}}(\theta) = \mathbb{E}_{t, \mathbf{x}_1, p_t(\mathbf{x}_t | \mathbf{x}_1)} [\beta(t)^2 \|\hat{\mathbf{x}}_1(\mathbf{x}_t, t; \theta) - \mathbf{x}_1\|^2 + \lambda(t)^2 \|\epsilon(\mathbf{x}_t, t; \theta) - \nabla_{\mathbf{x}} \log p_t(\mathbf{x}_t | \mathbf{x}_1)\|^2] \quad (27)$$

A.2 BALANCING THE IDFF FLOW

IDFF consists of a scoring model and an implicit flow component coupled with a parameter σ_0 to generate flow $\mathbf{w}(\cdot)$. We examine the effect of σ_0 on sample quality for the CIFAR-10 and CelebA datasets, with the NFE fixed at 10. As shown in Figure 4 (B), a value of $\sigma_0 = 0.6$ achieves the best balance between the diffusion and flow components regarding sample quality for both datasets. This plot also demonstrates that sample quality is susceptible to σ_0 , particularly for diffusion-based models like DDPMs, compared to CFMs, especially at small NFEs, which is already noticed in some research (Jolicœur-Martineau et al., 2020; Jain et al., 2020).

A.3 ON CONVERGENCE SPEED OF IDFF

IDFF introduces a momentum term that slightly increases training complexity compared to CFMs. However, this added complexity is offset by a significant reduction in the number of sampling steps required during inference. Leveraging the strengths of its underlying CFM models, IDFF achieves high-quality sample generation (FID < 10) within just 500K training iterations, as demonstrated in Figure 6, while maintaining competitive performance with CFMs.

Figure 6 shows the FID curves during IDFF training in the CIFAR-10 dataset with a batch size of 128, emphasizing its superior efficiency compared to conventional diffusion models. This efficiency

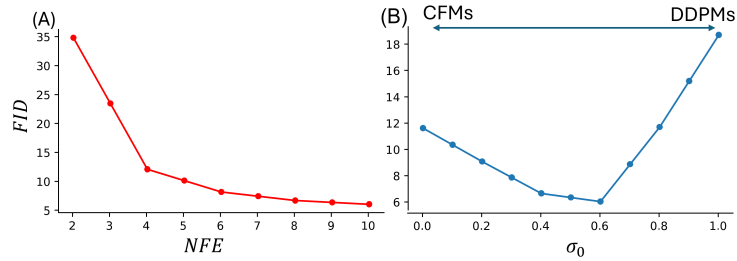


Figure 5: IDFF performance against A) the number of function evaluations (NFEs) and B) the hyperparameter σ_0 (the flow and score model mixing term) with fixed NFE=10, for CelebA-64 dataset.

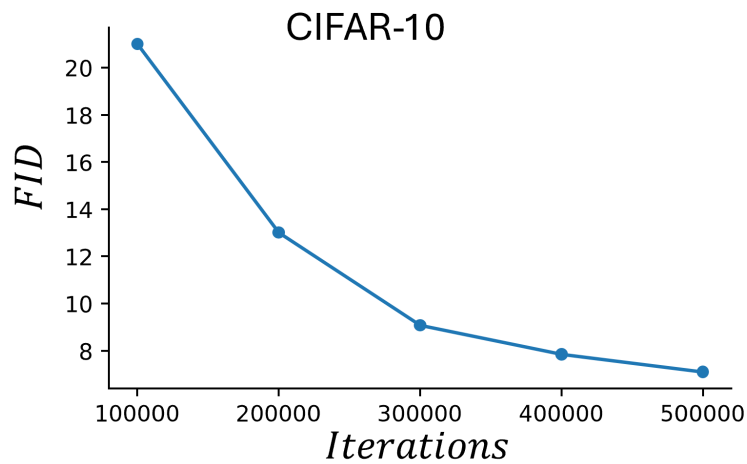


Figure 6: IDFF performance against the number of training iterations with fixed NFE=10 for the CIFAR-10 dataset.

marks a substantial improvement over the millions of iterations typically required by diffusion-based models to generate high-quality images, which entail considerable computational costs. In contrast, as depicted in Figure 6, IDFF retains the training efficiency of CFMs, achieving faster convergence and significant computational savings.

A.4 IDFF TRAINING AND SAMPLING ALGORITHMS FOR TIME SERIES

Algorithm 3 IDFF sampling algorithm for time-series data.

Input: $\hat{\mathbf{x}}_1(\cdot; \theta)$ and $\hat{\epsilon}(\cdot; \theta)$, maximum sequence length K , bandwidth σ_0 , time step size Δt , and γ .

for k in $\{1, \dots, K\}$ **do**

if $k == 1$ **then**

$\mathbf{x}_0^0 \sim \mathcal{N}(0, \mathbf{I})$

else

$\mathbf{x}_0^k \sim \mathcal{N}(\mathbf{x}_1^{k-1}, \sigma_0 \mathbf{I})$

end if

for t in $[0, 1/\Delta t)$ **do**

$\sigma_t \leftarrow \sigma_0 \sqrt{t(1-t)}$

$\mathbf{w}_t^k \leftarrow \sqrt{(1-\sigma_t^2)} \frac{\hat{\mathbf{x}}_1(\mathbf{x}_t, t, k; \theta) - \mathbf{x}_t^k}{1-t} + \frac{2\gamma-1}{2} \sigma_t \hat{\epsilon}(\mathbf{x}_t, t, k; \theta)$

$\mathbf{x}_{t+\Delta t}^k \sim \mathcal{N}(\mathbf{x}_t^k + \mathbf{w}_t^k \Delta t, \sigma_t^2 \Delta t \mathbf{I})$

end for

end for

return Samples $\{\mathbf{x}_1^k\}_{k=1}^K$

Algorithm 4 IDFF training algorithm for time-series data.

Input: dataset distribution $p_1(\mathbf{x}_1)$, initial distribution $p_0(\mathbf{x}_0)$, maximum sequence length K , bandwidth σ_0 , a set of positive weights $\lambda(\cdot)$ and $\beta(\cdot)$, initialized networks $\hat{\mathbf{x}}_1(\cdot; \theta)$ and $\hat{\epsilon}(\cdot; \theta)$,

while Training **do**

if $K == 1$ **then**

$k = 1$

$\mathbf{x}_1 \sim p_1(\mathbf{x}_1), \mathbf{x}_0 \sim p_0(\mathbf{x}_0)$

else

$k \sim \{1, \dots, K\}$ with equal probability

$\mathbf{x}_1 \sim p_1(\mathbf{x}_1^k), \mathbf{x}_0 \sim p_1(\mathbf{x}_1^{k-1})$

end if

$\pi \leftarrow \text{OT}(\mathbf{x}_1, \mathbf{x}_0)$

$(\mathbf{x}_0, \mathbf{x}_1) \sim \pi$

$t \sim \mathcal{U}(0, 1)$

$\boldsymbol{\mu}_t \leftarrow t\mathbf{x}_1 + (1-t)\mathbf{x}_0$

$\sigma_t \leftarrow \sigma_0 \sqrt{t(1-t)}$

$\mathbf{x}_t \sim \mathcal{N}(\boldsymbol{\mu}_t, \sigma_t^2 \mathbf{I})$

$\mathcal{L}_{\text{IDFF}}(\theta) \leftarrow \beta(t)^2 \|\hat{\mathbf{x}}_1(\mathbf{x}_t, t, k; \theta) - \mathbf{x}_1\|^2 + \lambda(t)^2 \|\epsilon(\mathbf{x}_t, t; \theta) - \nabla_x \log p_t(\mathbf{x}_t | \mathbf{x}_1)\|^2$

$\theta \leftarrow \text{Update}(\theta, \nabla_{\theta} \mathcal{L}(\theta))$

end while

return $\{\hat{\mathbf{x}}_1(\cdot; \theta), \hat{\epsilon}(\cdot; \theta)\}$

A.5 IMPLEMENTATION DETAILS

Network configuration: We adopt UNet (ADM) for our image generation and SST forecasting experiments. Table 5 shows detailed configurations of the ADM network on different datasets.

Training hyper-params. In Table 6, we provide training hyperparameters for unconditional image generation on ADM and SST forecasting datasets.

Table 5: ADM network configuration for different datasets.

	CIFAR-10	CelebA64	CelebA 256	Church & Bed	SST
# of ResNet blocks	2	2	2	2	2
Base channels	128	128	128	256	128
Channel multiplier	1,2,2,4	1,2,2,4,4	1,1,2,2,4,4	1,1,2,2,4,4	1,2,4
Attention resolutions	16	16	16	16	16
Label dimensions	1	1	1	1	10
Params (M)	65.6	102.14	453.45	108.41	55.39

Table 6: Hyper-parameters of ADM network.

	ImageNet-64	CIFAR-10	CelebA64	CelebA 256	Church & Bed	SST
lr	1e-4	1e-4	1e-5	1e-5	1e-5	1e-4
Batch size	64	128	128	16	16	8
# of iterations	3M	700K	1.2M	1.5M	1.5M	700K
# of GPUs	4	1	1	1	1	1

A.6 ADDITIONAL RESULTS FOR IMAGE GENERATION EXPERIMENT

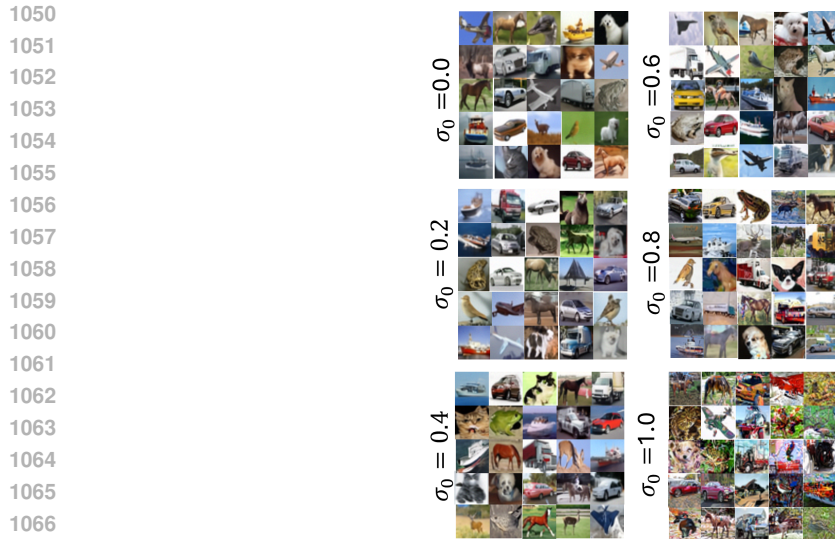
We also assess IDFF performance in generating images against fast diffusion process models with MFE=5. As Table 7 IDFF achieves a significantly better FID score (10.97) compared to UniPC (23.52) and DPM-Solver-v3 (12.21), while also boasting the fastest wall-clock time (0.34 seconds) among all solvers. This highlights IDFF’s ability to generate high-quality samples with minimal computational overhead, making it ideal for real-time applications. Even at NFE=10, where UniPC slightly edges out in FID (2.85) alongside DPM-Solver-v3 (2.91), IDFF remains competitive with a reasonable FID (5.87) and the fastest wall-clock time (0.52 seconds), demonstrating its efficiency and scalability. These results suggest that IDFF hits a balance between sample quality and computational speed that lends itself to speed.

Table 7: Comparison of FID↓ performance and sampling times (Wall-clock) between IDFF and fast diffusion sampling methods for NFE=5 and NFE=10, evaluated on 50k samples.

Method	FID (NFE=5)	Wall-clock (sec, NFE=5)	FID (NFE=10)	Wall-clock (sec, NFE=10)
UniPC (Zhao et al., 2024)	23.52	0.62	2.85	1.05
DPM-Solver-v3 (Zheng et al., 2023)	12.21	0.49	2.91	0.92
IDFF	10.97	0.34	5.87	0.52



1048 Figure 7: Generated samples for CelebA64 (64×64) dataset with different σ_0 s and $NFE = 10$.



1068 Figure 8: Generated samples for CIFAR-10 (32×32) dataset with different σ_0 s and $NFE = 10$.

1070 A.7 3D-ATTRACTORS

1072 In this experiment, we assess IDFF’s performance in generating trajectories of chaotic systems from
1073 scratch. We generate trajectories with $K = 2000$ samples in each trajectory from 3D attractors,
1074 specifically the Lorenz and Rössler attractors, which are chaotic systems with nonlinear dynam-
1075 ics. The parameters for the Lorenz and Rössler models are set to $\sigma = 10, \rho = 28, \beta = 8/3$ and
1076 $a = .2, b = .2, c = 5.7$, respectively, to produce complex trajectories in 3D space. We then train the
1077 IDFF model based on these trajectories. To model each attractor, we use an MLP with two hidden
1078 layers of 128 dimensions and two separate heads for $\hat{x}_1(\cdot, t, k; \theta)$ and $\epsilon(\mathbf{x}_t, t, k; \theta)$. Additionally, we
1079 incorporate two separate embedding layers for embedding t and k , which are directly concatenated
with the first hidden layer of the MLP. The optimized IDFF successfully generates samples of these



1121 Figure 9: Generated samples for CelebA-HQ (256×256) dataset with $\sigma_0 = 0.2$ and $NFE = 10$.
1122

1123
1124 trajectories from scratch. The generated trajectories are shown in Figure 13. The quality of the results
1125 demonstrates that IDFF can successfully simulate the behaviors of highly nonlinear and nonstationary
1126 systems such as attractors.

1127 1128 A.8 SST FORECASTING VISUALIZATION

1129 1130 A.9 2D-SIMULATED STATIC DATA AND TIME-SERIES

1131 Additional results for 2D simulations for both static and time-series generation are shown in Figure16.
1132
1133

1134
1135
1136
1137
1138
1139
1140
1141
1142
1143
1144
1145
1146
1147
1148
1149
1150
1151
1152
1153
1154
1155
1156
1157
1158
1159
1160
1161
1162
1163
1164
1165
1166
1167
1168
1169
1170
1171
1172
1173
1174
1175
1176
1177
1178
1179
1180
1181
1182
1183
1184
1185
1186
1187

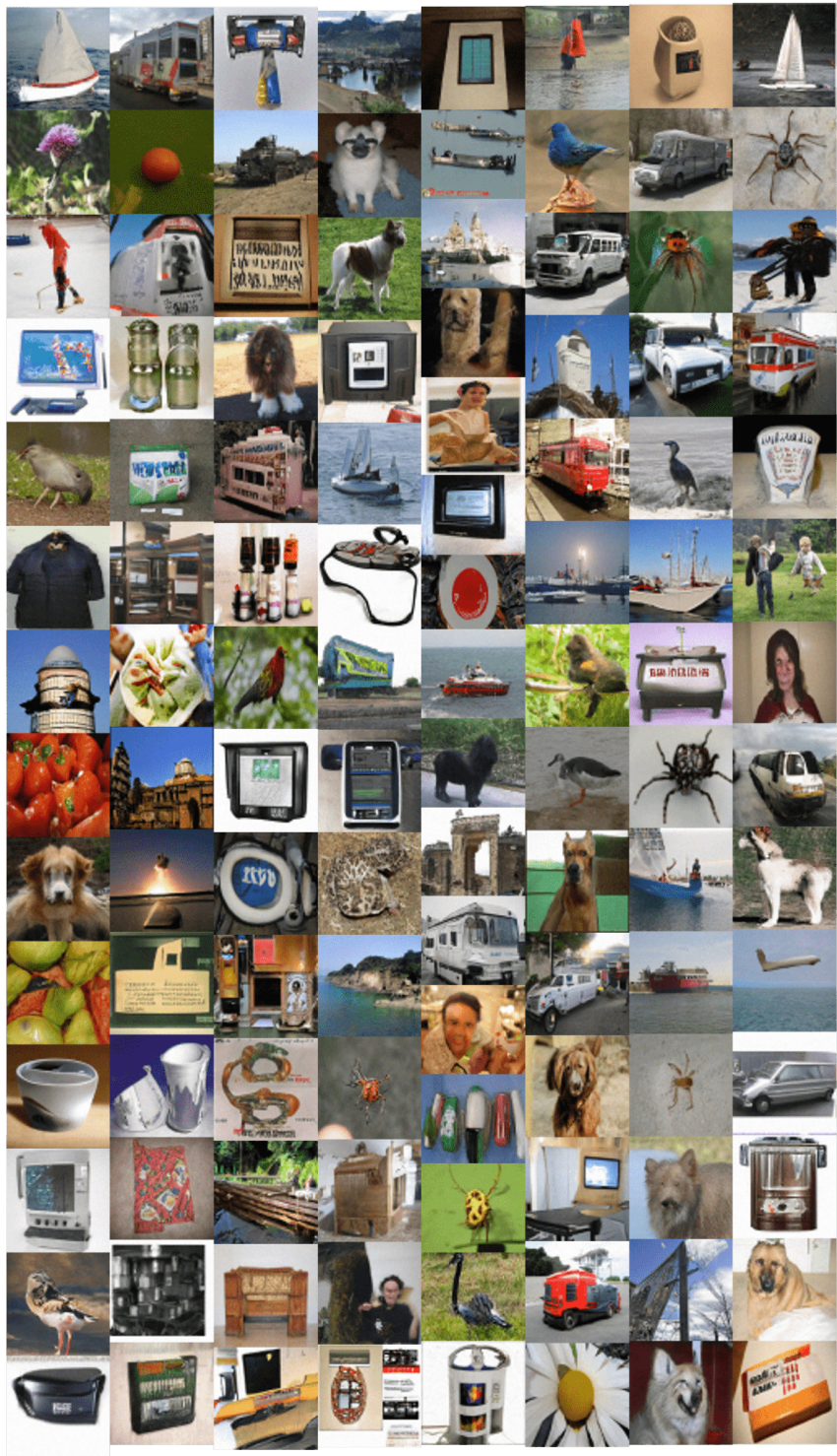


Figure 10: Generated samples for ImageNet64 dataset with $\sigma_0 = 0.2$ and $NFE = 10$.

1188
1189
1190
1191
1192
1193
1194
1195
1196
1197
1198
1199
1200
1201
1202
1203
1204
1205
1206
1207
1208
1209
1210
1211
1212
1213
1214
1215
1216
1217
1218
1219
1220
1221
1222
1223
1224
1225
1226
1227
1228
1229
1230
1231
1232
1233
1234
1235
1236
1237
1238
1239
1240
1241



Figure 11: Generated samples for LSUN-church (256×256) dataset with different σ_0 s and $NFE = 10$.

1242
1243
1244
1245
1246
1247
1248
1249
1250
1251
1252
1253
1254
1255
1256
1257
1258
1259
1260
1261
1262
1263
1264
1265
1266
1267
1268
1269
1270
1271
1272
1273
1274
1275
1276
1277
1278
1279
1280
1281
1282
1283
1284
1285
1286
1287
1288
1289
1290
1291
1292
1293
1294
1295



Figure 12: Generated samples for LSUN-bed (256×256) dataset with different σ_0 s and $NFE = 10$.

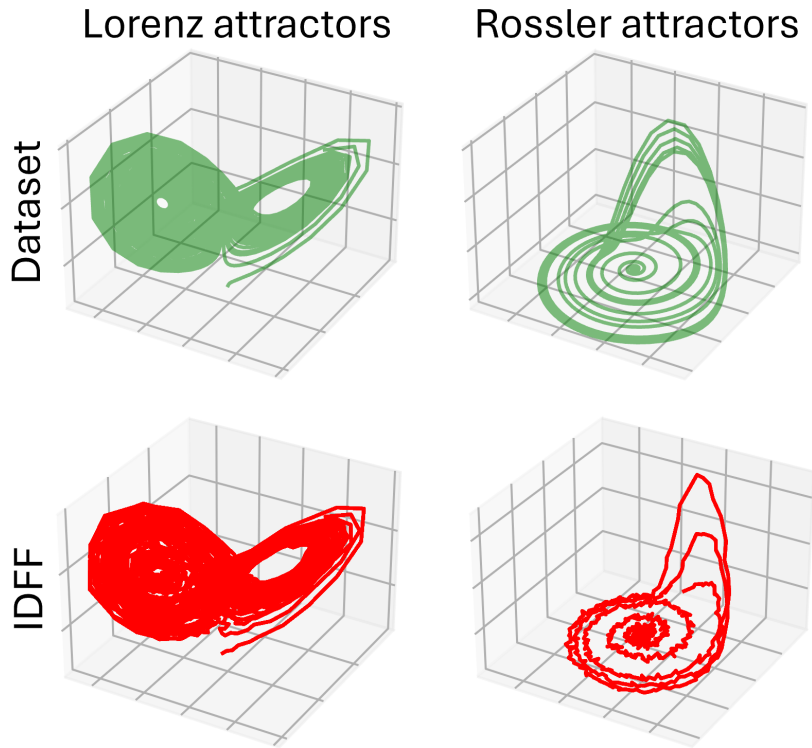
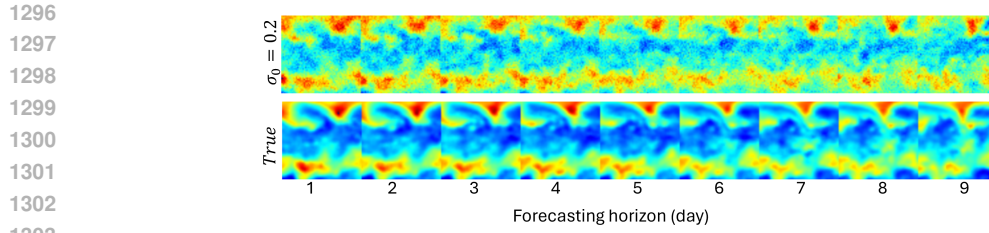
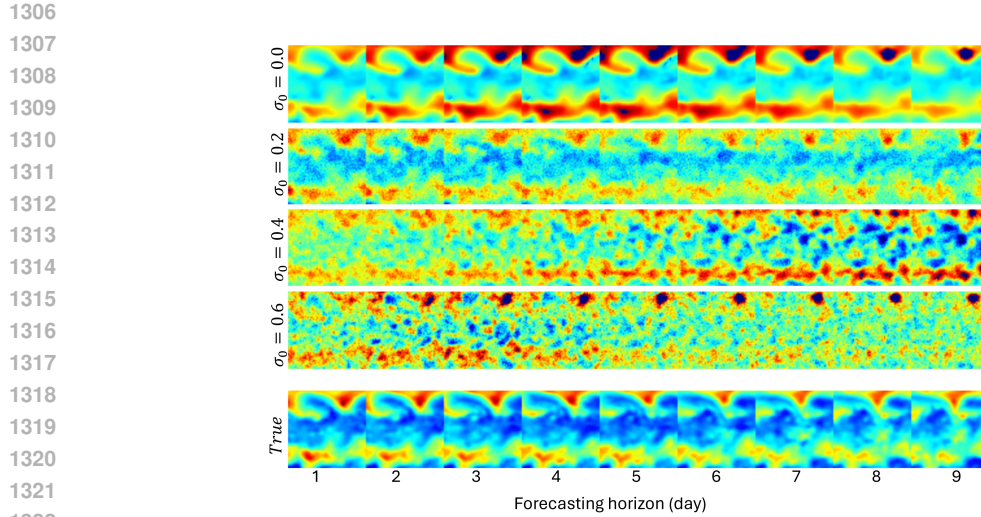


Figure 13: Time-series simulation. IDFF trajectory generation for the chaotic systems.



1304 Figure 14: SST forecasting result conditioned on day 1st for 9 days with $\sigma_0 = 0.2$ and fixed
1305 $NFE = 5$. Same results for different σ_0 s is shown in Figure15



1323 Figure 15: SST forecasting result conditioned on day 1st for 9 days for different values of σ_0 and
1324 fixed $NFE = 5$.

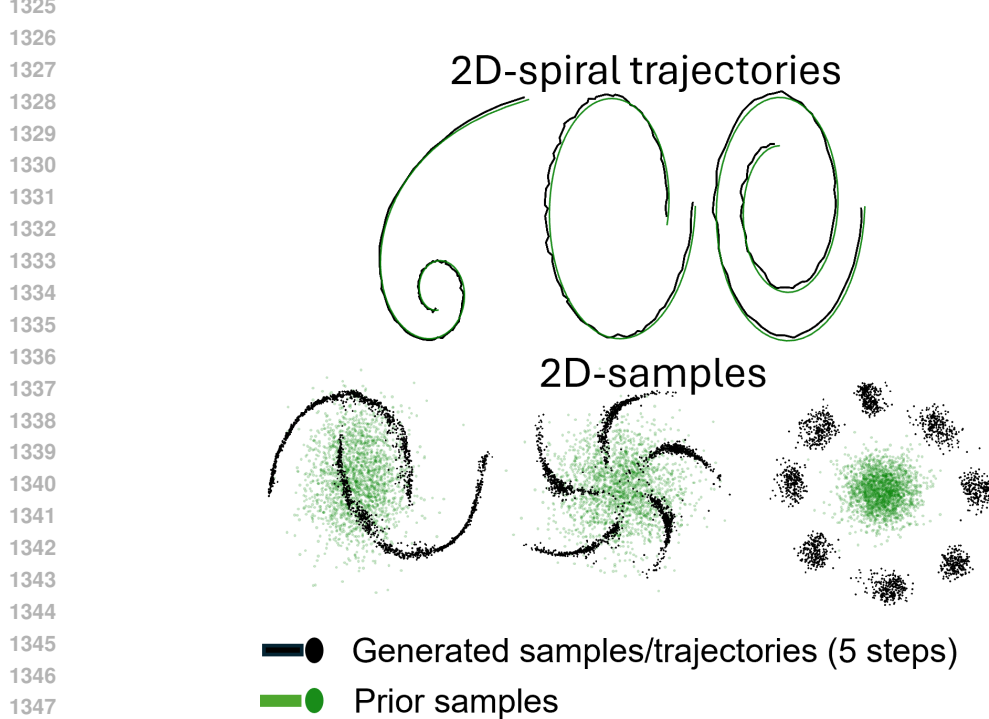


Figure 16: 2D synthetic simulation.